Supplementary Information

Fast Mg-ion insertion kinetics in V_2Se_9

Author details

Corresponding Authors

Laurence J. Hardwick – *Department of Chemistry, University of Liverpool, Liverpool, L69 7ZD, UK, Stephenson Institute for Renewable Energy, University of Liverpool, Liverpool L69 7ZF, UK, The Faraday Institution, Harwell Campus, Didcot, OX11 0RA,* orcid.org/0000-0001-8796-685X*;* email*:* hardwick@liverpool.ac.uk

Matthew J. Rosseinsky – *Department of Chemistry, University of Liverpool, Liverpool, L69 7ZD, UK,* orcid.org/ 0000-0002-1910-2483; email: M.J.Rosseinsky@liverpool.ac.uk

Authors

Matthew A. Wright – *Department of Chemistry, University of Liverpool, Liverpool, L69 7ZD, UK, Stephenson Institute for Renewable Energy, Liverpool L69 7ZF, UK, Present Address: Materials Research Laboratory, Materials Department, University of California, Santa Barbara, California, CA 93106, USA,* orcid.org/0000-0003-0617-3992

Jungwoo Lim – *Department of Chemistry, University of Liverpool, Liverpool, L69 7ZD, UK, Stephenson Institute for Renewable Energy, University of Liverpool, Liverpool L69 7ZF, UK, The Faraday Institution, Harwell Campus, Didcot, OX11 0RA, UK,* orcid.org/0000-0002-4123-2882

Raul A. Pacheco Muino – *Department of Chemistry, University of Liverpool, Liverpool, L69 7ZD, UK, Present Address: Department of Chemistry, Imperial College London, London, W12 0BZ, UK,* orcid.org/0000-0006-7711-3435

Anna E. Krowitz – *Department of Chemistry, University of Liverpool, Liverpool, L69 7ZD, UK,* orcid.org/0009-0002-7717-2049

Cara J. Hawkins – *Department of Chemistry, University of Liverpool, Liverpool, L69 7ZD, UK,* orcid.org/0009-0001-0927-9808

Mounib Bahri – *Albert Crewe Centre, University of Liverpool, Research Technology Building, Elisabeth Street, Pembroke Place, Liverpool, L69 3GE, UK; School of Engineering, Department of Mechanical, Materials and Aerospace Engineering, University of Liverpool, Liverpool, L69 3GH, UK,* orcid.org/0000-0002-8336-9158

Luke M. Daniels – *Department of Chemistry, University of Liverpool, Liverpool, L69 7ZD, UK,* orcid.org/0000-0002-7077-6125

Ruiyong Chen – *Department of Chemistry, University of Liverpool, Liverpool, L69 7ZD, UK,* orcid.org/0000-0002-5340-248X

Luciana G. Chagas – *Johnson Matthey Technology Centre, Sonning Common, Reading, RG4 9NH, UK*

James Cookson – *Johnson Matthey Technology Centre, Sonning Common, Reading, RG4 9NH, UK*

Paul Collier – *Johnson Matthey Technology Centre, Sonning Common, Reading, RG4 9NH, UK*

Supplementary Information

Alan V. Chadwick – *School of Physical Science, University of Kent, Canterbury, CT2 7NH, UK,* orcid.org/0000-0002-6485-9207

Nigel D. Browning – *Albert Crewe Centre, University of Liverpool, Research Technology Building, Elisabeth Street, Pembroke Place, Liverpool, L69 3GE, UK; School of Engineering, Department of Mechanical, Materials and Aerospace Engineering, University of Liverpool, Liverpool, L69 3GH, UK,* orcid.org/0000-0003-0491-251X

John B. Claridge – *Department of Chemistry, University of Liverpool, Liverpool, L69 7ZD, UK,* orcid.org/0000-0003-4849-6714

Structure of V_2Se_9

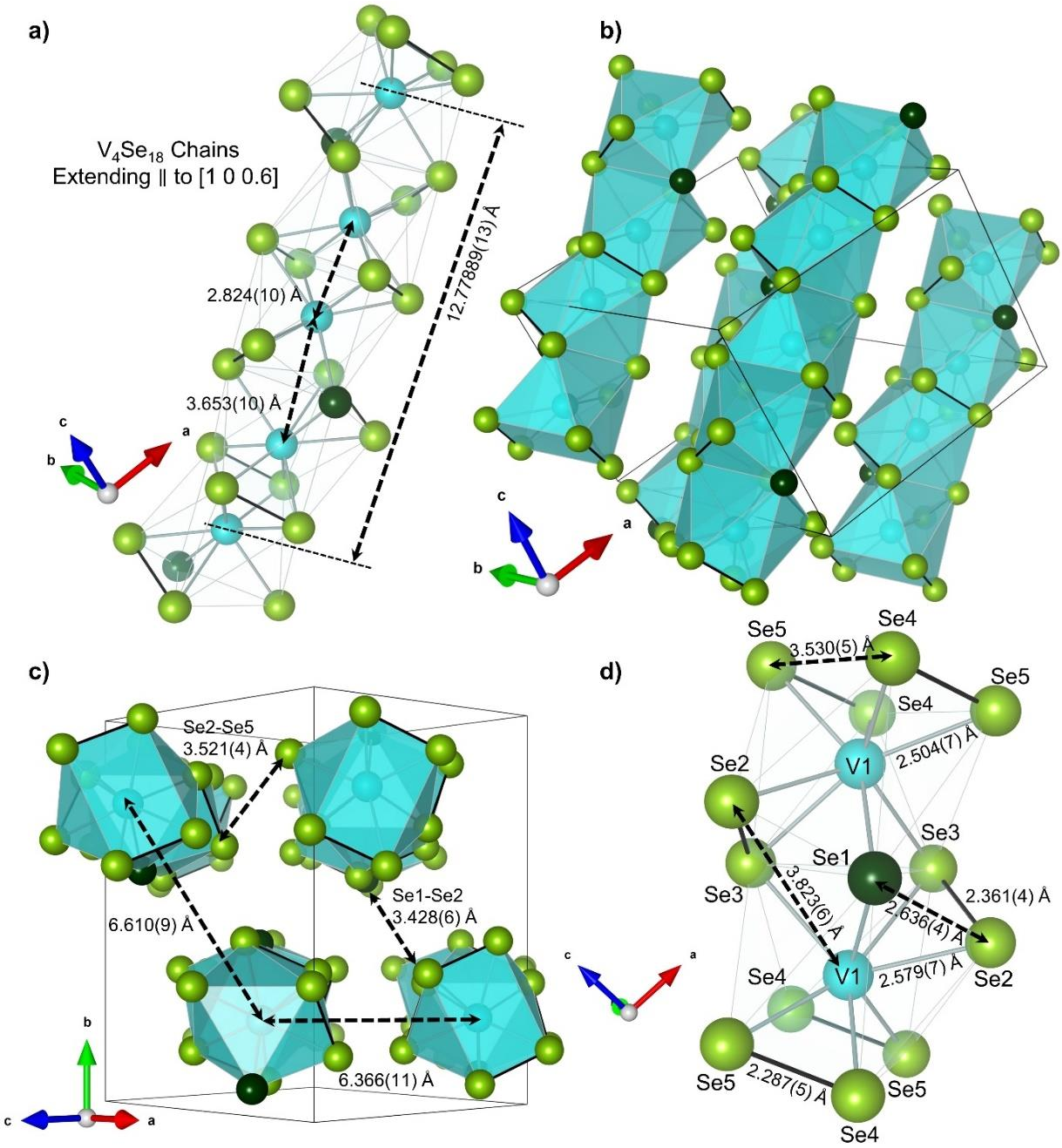

Figure S1 V_2Se_9 crystallizes in *C2/c* symmetry. The structure of V_2Se_9 is one dimensional and closely resembles that of VS_4.[1] Vanadium is shown by blue spheres, selenium by green. Light green denotes Se

in a 1- oxidation state $(Se_2)^{2-}$ and dark green denotes Se in a 2- oxidation state. Se–Se bonds are shown by black lines and V–Se is shown by light grey lines. Distorted rectangular antiprism $[VSe_8]$ polyhedra are shown in light blue. Select bond lengths and interatomic distances are provided. a) V_2Se_9 consists of separate $[V_4Se_{18}]_n$ chains that extend in the [302] direction with a translation period of 12.77889(13) Å to form needle-like crystallites. Pairs of vanadium sites are observed along the chains with the distance between two centrosymmetric equivalent sites being 2.824(10) Å. The shortest distance between two vanadium atoms related to each other by a two-fold axis is 3.653(10) Å. b-c) A unit cell of V_2Se_9 contains four parallel $[V_4Se_{18}]_n$ chains that are bound together through weak Van der Waals interactions. The bonding between individual chains is weak, with the shortest inter-chain Se–Se distances being 3.428(6) Å (Se1–Se2) and 3.521(4) Å (Se2–Se5); and the shortest inter-chain V–V distances being 6.366(11) Å and 6.610(9) Å, in the [-102] and [011] directions, respectively. This anisotropy is observed in the splitting of crystallites into needles parallel to the chain direction. d) Asymmetric unit of V_2Se_9 with select bond lengths. Locally, each vanadium occupies an eight-coordinate environment with selenium forming distorted rectangular anti-prismatic $[VSe_8]$ polyhedral with an internal volume of 29.052 $Å^3$. Select distances are provided in Table S1. Seven of the selenium anions form four diselenide, $(Se_2)^{2-}$, units around the metal centre. The corners of the rectangular face of the antiprism between centrosymmetrically equivalent vanadium is formed by two $(Se_2)^{2-}$. The Se4–Se5 bond length is 2.287(5) Å which is in agreement the ideal Se–Se bond length, R_o, of 2.33 Å[2,3] and with distances reported in other materials containing $(Se_2)^{2-}$, such as $NbSe_3$ (2.37 Å) and Nb_2Se_9 (2.30-2.36 Å).[4,5] The Se–Se bonds in the $(Se_2)^{2-}$ units of V_2Se_9 are longer than S–S in $(S_2)^{2-}$ units, which are 2.03-2.04 Å in VS_4. The interatomic distance between non-bonded Se4–Se5 is 3.530(5) Å and the average V–Se distance is 2.575 Å (with a range of 2.504(7)-2.664(6) Å). Additional $(Se_2)^{2-}$ bonds are formed between Se2–Se3 with a bond length of 2.361(4) Å. Se3 is coordinated to two separate vanadium centres that are related by a two-fold axis with V–Se3 bond lengths of 2.648(6) Å and 2.664(6) Å. Se2 is coordinated to only one vanadium metal centre with a V–Se bond length of 2.579(7) Å and a much larger distance of 3.823(6) Å to the non-coordinated vanadium. The single Se^{2-} anion Se1 is situated on a two-fold axis and is also coordinated to the two vanadium metal centres, with a V–Se1 bond length of 2.578(4) Å. Se1 is not bonded to selenium; an interatomic distance of 2.636(7) Å from Se2 (the nearest Se sites) is beyond the reasonable limit of Se–Se bonding; Se1 therefore has a 2- oxidation state. The different oxidation states in V_2Se_9 can be written as $V_2^{5+}(Se_2)^{2-}{}_4Se^{2-}$: vanadium is present as V^{5+}; eight selenium anions form four $(Se_2)^{2-}$, each of formal oxidation state of 1-; and Se1 with an oxidation state of 2-.

Table S1 Select interatomic distances in V_2Se_9.

Interatomic Distance (Å)		Interatomic Distance (Å)		Interatomic Distance (Å)	
V-V	2.824(10)	Se1-Se2	2.636(4)	Se3-V	2.664(6)
V-V	3.653(10)	Se1-V	2.578(6)	Se4-V	2.544(6)
Se2-Se3	2.361(4)	Se2-V	3.823(6)	Se4-V	2.542(6)
Se4-Se5	2.287(5)	Se2-V	2.579(7)	Se5-V	2.504(7)
Se4-Se5	3.530(5)	Se3-V	2.648(6)	Se5-V	2.523(6)

Supplementary Information

Rietveld Refinement against SXRD Data for V_2Se_9

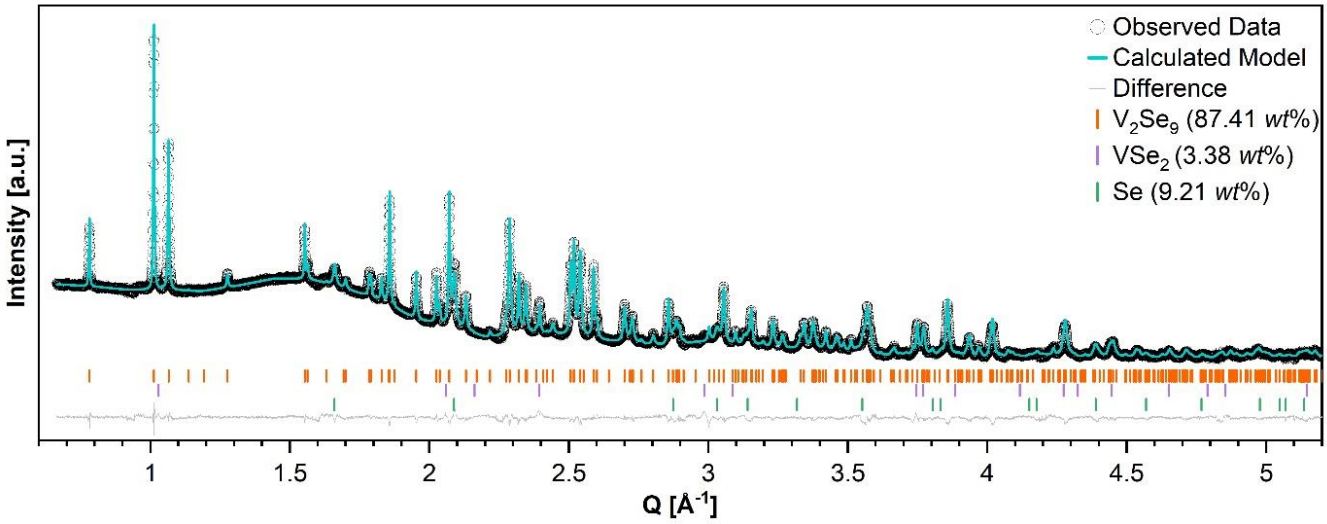

Figure S2 Rietveld refinement of V_2Se_9 against SXRD data collected at the I11 beamline. White circles show observed data. The cyan line shows the calculated fit. The difference between the calculated and observed data is shown by the grey line. The *hkls* of V_2Se_9, VSe_2 and Se are given by the orange, purple and green ticks, respectively. Refined parameters are summarized in Table S2.

Table S2 Rietveld parameters for V_2Se_9 with refined lattice parameters, atomic coordinates, and isotropic displacement parameters against SXRD.

C 2/*c*	R_{wp} = 0.62%	R_p = 0.43 %	G.O.F = 7.08				
Atom	Oxidation state	Wykoff	x	y	z	Occ	B_{iso} [Å^2]
V1	V^{5+}	8f	0.1311(4)	0.2322(2)	0.4116(5)	1.00	0.50(10)
Se1	Se^{2-}	4e	0	0.0856(3)	0.25	1.00	0.65(16)
Se2	Se^{1-}	8f	0.4384(2)	0.3487(2)	0.0413(3)	1.00	1.39(10)
Se3	Se^{1-}	8f	0.1032(2)	0.3122(2)	0.1082(3)	1.00	0.85(10)
Se4	Se^{1-}	8f	0.2636(2)	0.0836(2)	0.5560(3)	1.00	0.91(10)
Se5	Se^{1-}	8f	0.3348(2)	0.1583(2)	0.3236(3)	1.00	0.20(9)

a = 10.58876(10) Å

b =12.40942(18) Å

c = 8.12006(8) Å

β = 94.9229(8)°

Volume = 1063.04(2) Å^3

Supplementary Information

ICP-OES Data for V_2Se_9

Inductively Coupled Plasma Optical Emission Spectroscopy (ICP-OES) was used to determine the elemental composition by digesting ≈5 mg of samples in ≈1 mL aqua regia and diluting with ultra-pure water to appropriate concentrations (generally 10-150 ppm).

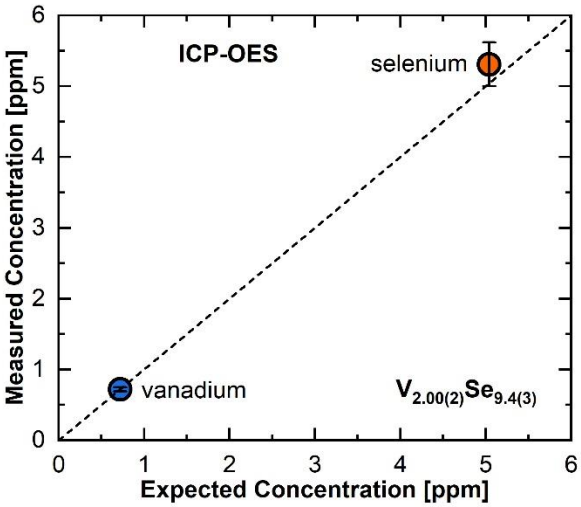

Figure S3 ICP-OES of V_2Se_9. Measured concentration in ppm of each element is plotted as a function of calculated (expected) concentration in ppm with errors shown by vertical bars. The dashed line represents $y = x$ as corresponds to the union between expected and measured values. Measured values are provided in Tables S3 and S4, respectively.

Table S3 ICP-OES data collected on V_2Se_9 bulk powder: measured composition $V_{2.00(2)}Se_{9.4(3)}$.

Element	MW [g/mol]	Concentration As Weighed [mg/L]	Measured Concentration [mg/L]	%RSD
V (268.796 nm)	50.94	0.72	0.74	0.65
V (292.401 nm)	50.94	0.72	0.68	0.47
V(309.310 nm)	50.94	0.72	0.74	0.51
V (311.837 nm)	50.94	0.72	0.73	0.54
Se (196.026 nm)	78.96	5.04	5.53	0.23
Se (203.985 nm)	78.96	5.04	5.09	0.53

Supplementary Information

TEM Microscopy Images and EDX Data for V_2Se_9

Transmission electron microscopy (TEM) was performed at 200kV on a JEOL 2100+ equipped with a GATAN Rio Camera. Energy Dispersive X-ray spectroscopy (EDX) data were collected on the same microscope using an X-Max detector from Oxford instruments. Powder samples were dispersed on carbon coated TEM grids. The sample transfer to the TEM was performed using a GATAN 648 double tilt, beryllium vacuum transfer holder. EDX correction factors, for the different elements, were estimated measuring the EDX spectra of appropriate standards. Standard purity was confirmed using X-ray diffraction and electron microscopy. Quantification was performed using Aztec software.

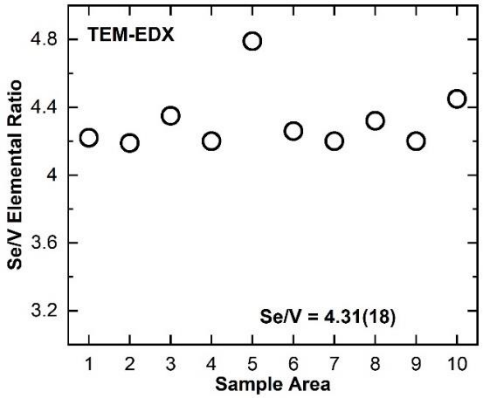

Figure S4 TEM-EDX of V_2Se_9 was used to measure the sample composition and homogeneity in ten separate crystallites. A Se/V ratio of 4.31(18) was measured.

Table S4 TEM-EDX results for vanadium and selenium content of V_2Se_9 bulk powder.

Sample Area	Normalized Se	Normalized V	Sum	Se/V Ratio
1	80.87	19.13	100.00	4.23
2	80.77	19.23	100.00	4.20
3	81.31	18.69	100.00	4.35
4	80.76	19.24	100.00	4.20
5	82.74	17.26	100.00	4.79
6	80.98	19.02	100.00	4.26
7	80.76	19.24	100.00	4.20
8	81.20	18.80	100.00	4.32
9	80.76	19.24	100.00	4.20
10	81.64	18.36	100.00	4.45

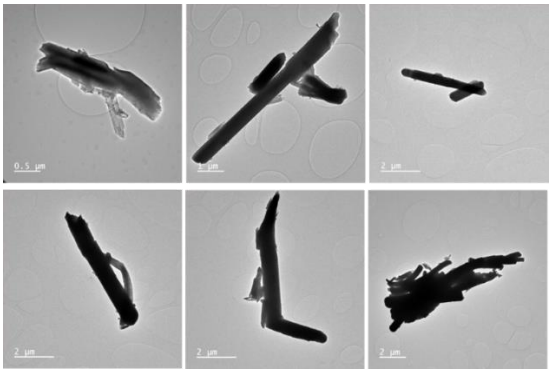

Figure S5 TEM images of V_2Se_9 crystallites with rod-like morphologies. Scale bar is displayed in the bottom left of each image.

Supplementary Information

Electrolyte Preparation: 0.5 M $Mg(TFSI)_2$ in Dimethoxyethane/and 1-methoxy-2-propylamine

Figures S6-8 and Table S5 are adapted from data presented in our recent publication and are included for clarity regarding the Mg electrochemistry testing protocol.[6]

bis((trifluoromethyl)sulfonyl)amide 1-methoxy-2-propylamine

Figure S6 Chemical structures of bis(trifluoromethane)sulfonimide and 1-methoxy-2-propylamine.

Table S5 gives the water content of the liquid components of the 0.5 M $Mg(TFSI)_2$ / DME-MPA electrolyte after various drying stages.

	<H_2O Content> by Karl-Fischer (ppm)			
Reagent	As purchased	CaH_2 distillation	Further drying (4 Å molecular sieves)	Second drying (4 Å molecular sieves)
Dimethoxyethane	28	NA	11.4(3)	9.4(15)
1-methoxypropyl-2-amine	> 1000	25(1)	12.2(10)	9.5(10)

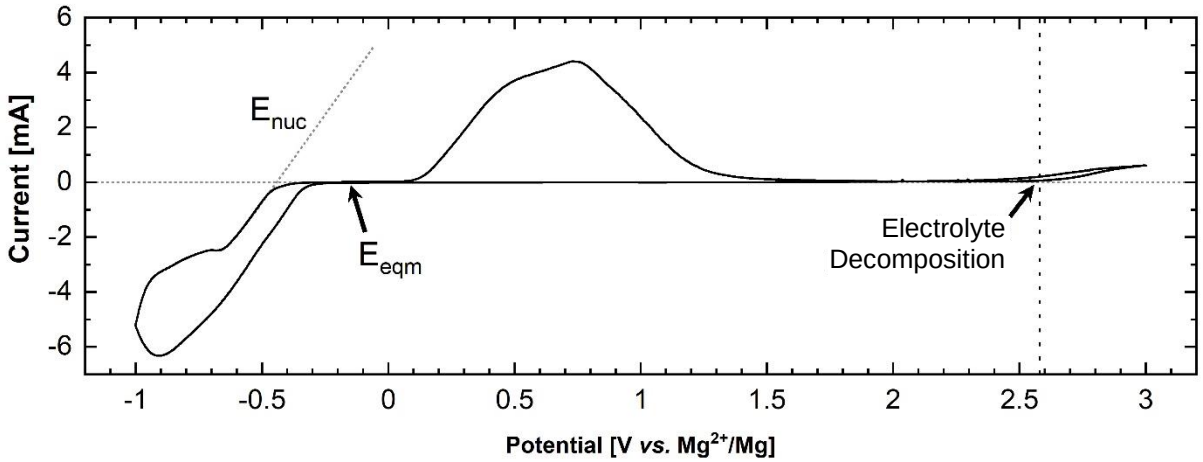

Figure S7 Second cycle cyclic voltammograms of Mg plating and stripping at a sweep rate of 0.01 V s^{-1} in 0.5M $Mg(TFSI)_2$/DME-MPA between -1.0 and 3.0 V *vs.* Mg^{2+}/Mg using a carbon coated aluminium working electrode with the integrated areas for plating (blue), stripping (gold), and solvent oxidation (grey). Plating occurs at potentials below the Nernst equilibrium potential (E_{eqm}). The Nucleation potential (E_{nuc}) corresponds to the potential below which nucleation of Mg metal occurs on the surface of the electrode.[7] The over-potential for Mg deposition was 0.224 V, close to what is reported in the literature and significantly smaller than standard $Mg(TFSI)_2$/DME (approximately 2.0 V).[8] CV data provides an onset of the electrochemical oxidation stability of the electrolyte (2.6 V vs. Mg^{2+}/Mg).

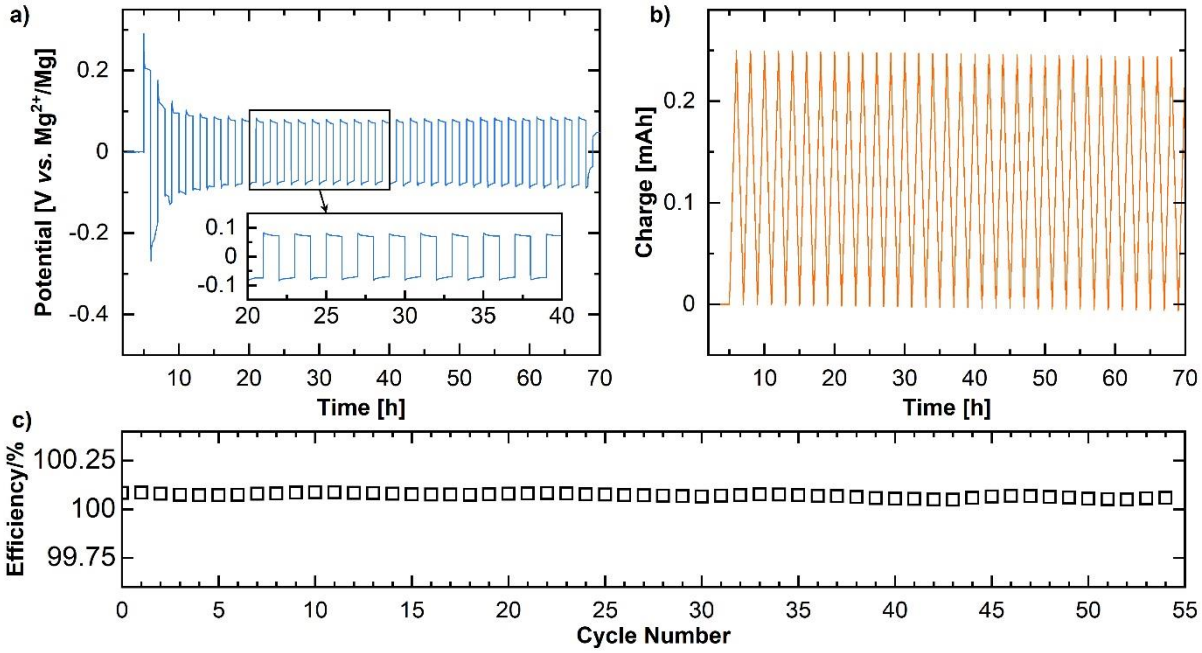

Figure S8 Galvanostatic cycling of a Mg-Mg symmetric cell at a current density of 0.5 mA cm^{-2}. (a) Potential *vs.* time plot, inset shows the voltage profiles between 0.2 and -0.2 V. (b) Charge *vs.* time plot. (c) Coulombic efficiency is maintained at 100.0(8) % for 55 cycles. The efficiency of plating and stripping was assessed for 0.5M $Mg(TFSI)_2$ in DME/MPA by galvanostatically cycling a Mg|electrolyte|Mg symmetric cell at a current density of 0.5 mA cm^{-2}. A second cycle over-potential of 0.177 V, which decreased to 0.082 V by cycle 10. A columbic efficiency of 100.0(8) % was calculated from the charge transferred during each plating-stripping cycle.

Electrochemical Characterization of $Mg_xV_2Se_9$

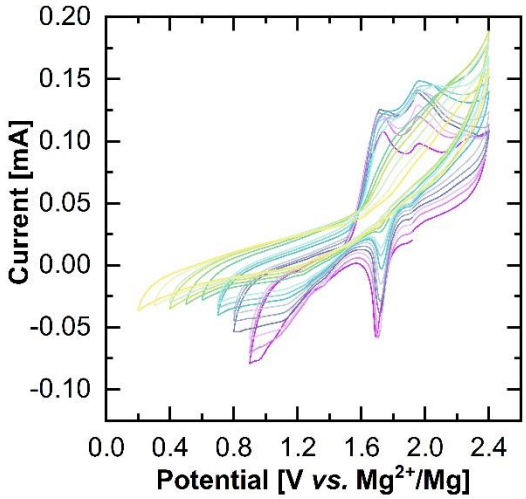

Figure S9 Cyclic voltammetry of V_2Se_9 in 0.5 M $Mg(TFSI)_2$ in dimethoxyethane/1-methoxypropyl-2-amine (3.84/1 w/w) at a sweep rate of 0.1 mV s^{-1}. The oxidative switching potential is 2.42 V. The reductive switching potential is decreased from 0.9 V to 0.2 V in 0.1 V increments. Loss of cyclable redox is observed almost immediately when the potential is swept below 0.7 V.

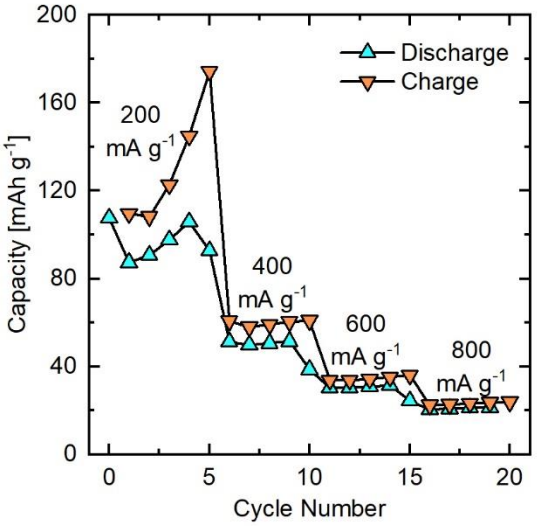

Figure S10 Discharge capacity (cyan triangles) and charge capacity (orange triangles) achieved over 20 cycles at current densities of 200-800 mA g^1.

Supplementary Information

Ex Situ Analysis of $Mg_{1.35}V_2Se_9$

Table S6 ICP-OES data collected for $Mg_{1.35}V_2Se_9$: composition measured as $Mg_{1.20(3)}V_{2.00(8)}Se_{9.4(5)}$.

Element	MW [g/mol]	Measured Concentration [mg/L]	%RSD
Mg (279.078 nm)	24.305	0.21	1.45
Mg (279.800 nm)	24.305	0.2	1
Mg (383.829 nm)	24.305	0.21	0.58
V (268.796 nm)	50.94	5.53	0.23
V (292.401 nm)	50.94	5.09	0.53
V(309.310 nm)	50.94	0.73	0.65
V (311.837 nm)	50.94	0.74	0.47
Se (196.026 nm)	78.96	0.68	0.51
Se (203.985 nm)	78.96	0.74	0.54

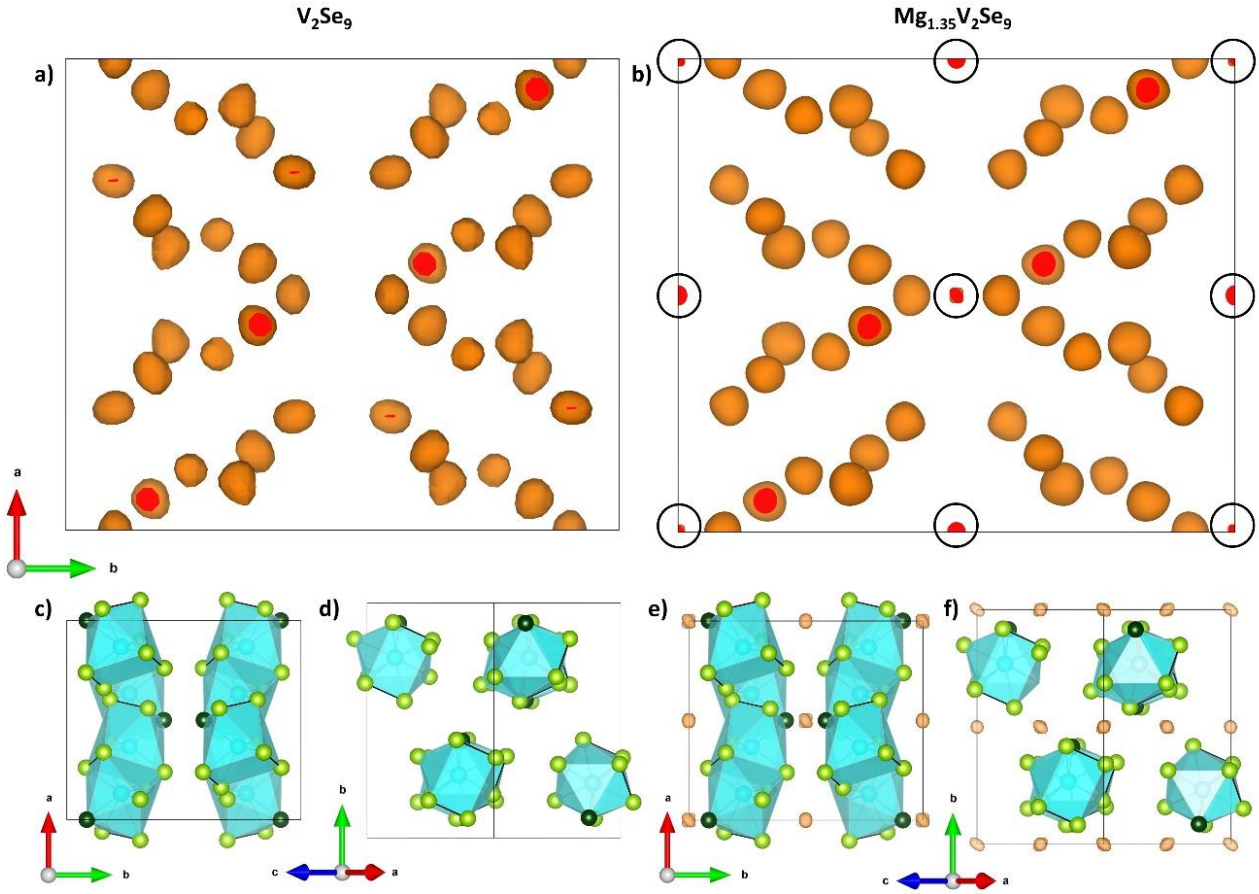

Figure S11 Electron density maps of (a) V_2Se_9 and (b) $Mg_{1.35}V_2Se_9$ generated by Fourier difference analysis of SXRD data. Areas of additional electron density for $Mg_{1.35}V_2Se_9$ are highlighted by black circles. (c-d) Fourier observed map for V_2Se_9 overlaid with the structure of V_2Se_9 showing no residual electron density between chains. (e-f) Fourier observed map for $Mg_{1.35}V_2Se_9$ overlaid with the structure of $Mg_{1.35}V_2Se_9$ showing electron density between chains that is not previously observed for V_2Se_9.

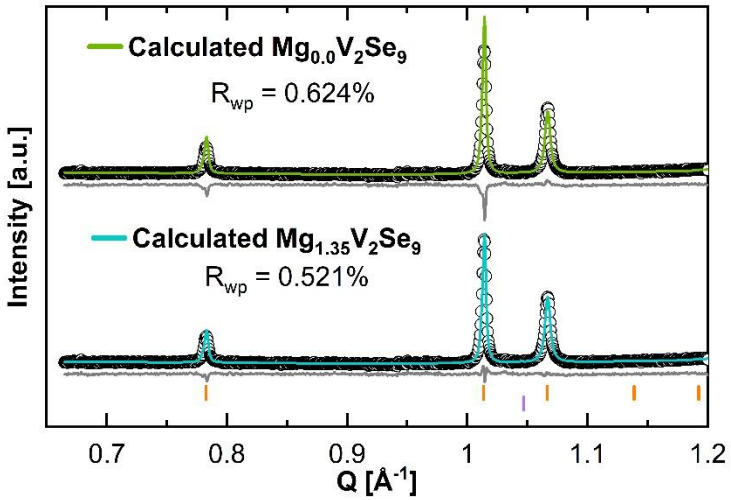

Figure S12 Rietveld refinement of $Mg_xV_2Se_9$ (x = 0.00, 1.35) against SXRD data collected at the I11 beamline; (top) Mg is not included in the structure ($Mg_{0.00}V_2Se_9$), yielding an R_{wp} of 0.624 %, (bottom) Mg(1) and Mg(2) site occupancies have been refined to 0.596(19) and 0.402(16), respectively, ($Mg_{1.35}V_2Se_9$) yielding an R_{wp} of 0.521 %. Observed data are shown by white circles. The calculated fit is shown by the green line for $Mg_{0.00}V_2Se_9$ and the cyan line for $Mg_{1.35}V_2Se_9$. The difference between the calculated and observed data is shown by the grey line. The Bragg reflection positions of V_2Se_9, VSe_2 and Se are given by the orange, purple and green ticks, respectively.

Table S7 Refined parameters from Rietveld refinement against SXRD data on $Mg_{1.35}V_2Se_9$ with refined lattice parameters, atomic coordinates, and isotropic displacement parameters. The total refined Mg content is 0.99(3).

C 2/*c*		R_{wp} = 0.52%		R_p = 0.36 %	G.O.F = 3.39		
Atom	Oxidation	Wykoff	x	y	z	Occ	B_{iso} (Å^2)
Mg1	Mg^{2+}	4a	0	0.5	0	0.596(19)	3.00(11)
Mg2	Mg^{2+}	4b	0.5	0.5	0	0.402(16)	3.00(11)
V1	V^{5+}	8f	0.1252(5)	0.2295(3)	0.4103(7)	1.00	1.35(12)
Se1	Se^{2-}	4e	0	0.0834(5)	0.25	1.00	0.87(18)
Se2	Se^{1-}	8f	0.4381(3)	0.3473(3)	0.0405(4)	1.00	0.96(11)
Se3	Se^{1-}	8f	0.1062(3)	0.3096(3)	0.1098(3)	1.00	1.54(12)
Se4	Se^{1-}	8f	0.2633(2)	0.0901(3)	0.5576(4)	1.00	0.91(12)
Se5	Se^{1-}	8f	0.3317(4)	0.1606(3)	0.3190(5)	1.00	1.28(11)

a = 10.57700(9) Å

b = 12.39645(10) Å

c = 8.11045(10) Å

β = 94.9145(10)°

Volume = 1059.511(18) Å^3

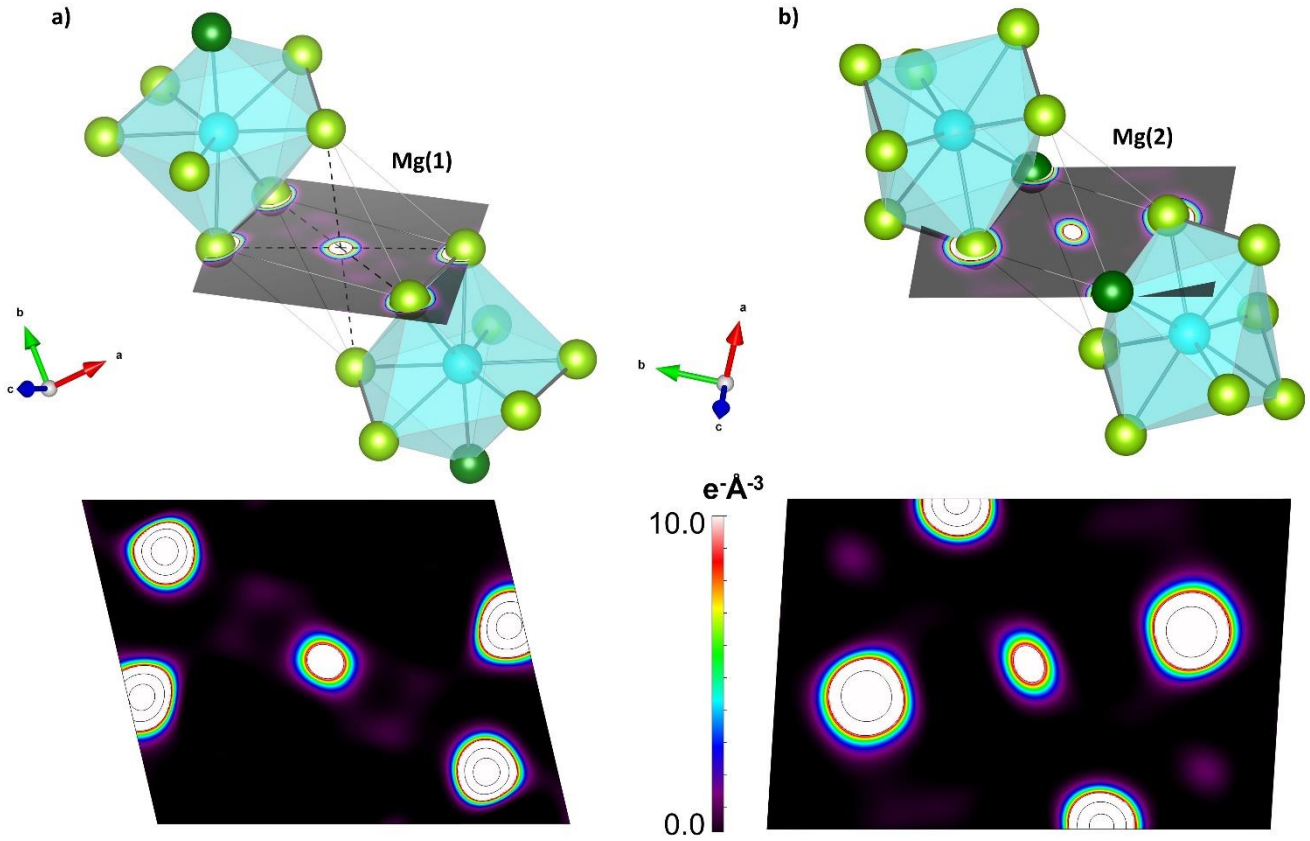

Figure S13 Maximum entropy method calculations were performed on observed SXRD to evaluate the electron density of $Mg_{1.35}V_2Se_9$. High-resolution 300×300×300 voxel maps provide resolution of 25.5k voxels $Å^{-3}$; with an individual voxel representing electron density for a volume of 3.9×10^{-5} $Å^3$. 2D slices taken in the (0.55 1.1 0.5) plane at 6.53 Å from the origin and (7 2 1) plane at 7.09 Å from the origin depict cross-sections of the (a) Mg(1) an (b) Mg(2) octahedra, respectively, dissecting their equatorial bonding plane.

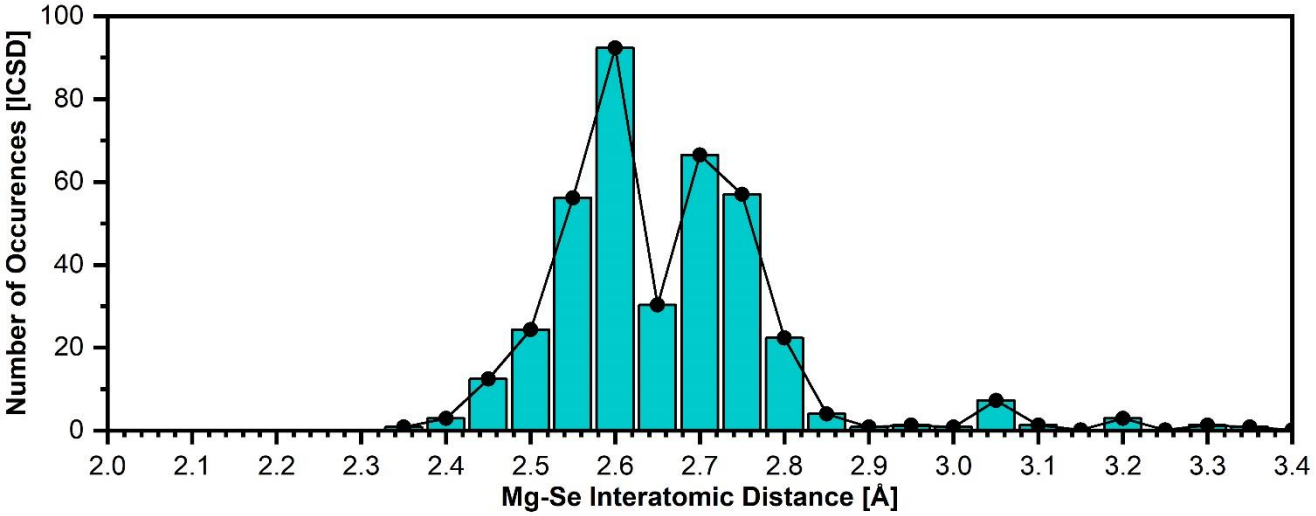

Figure S14 Frequency of reported Mg–Se interatomic distances in the ICSD as of April 2024. The ideal Mg-Se bond distance is reported as 2.32 $Å^3$ with a distribution of 2.4-2.9 Å.

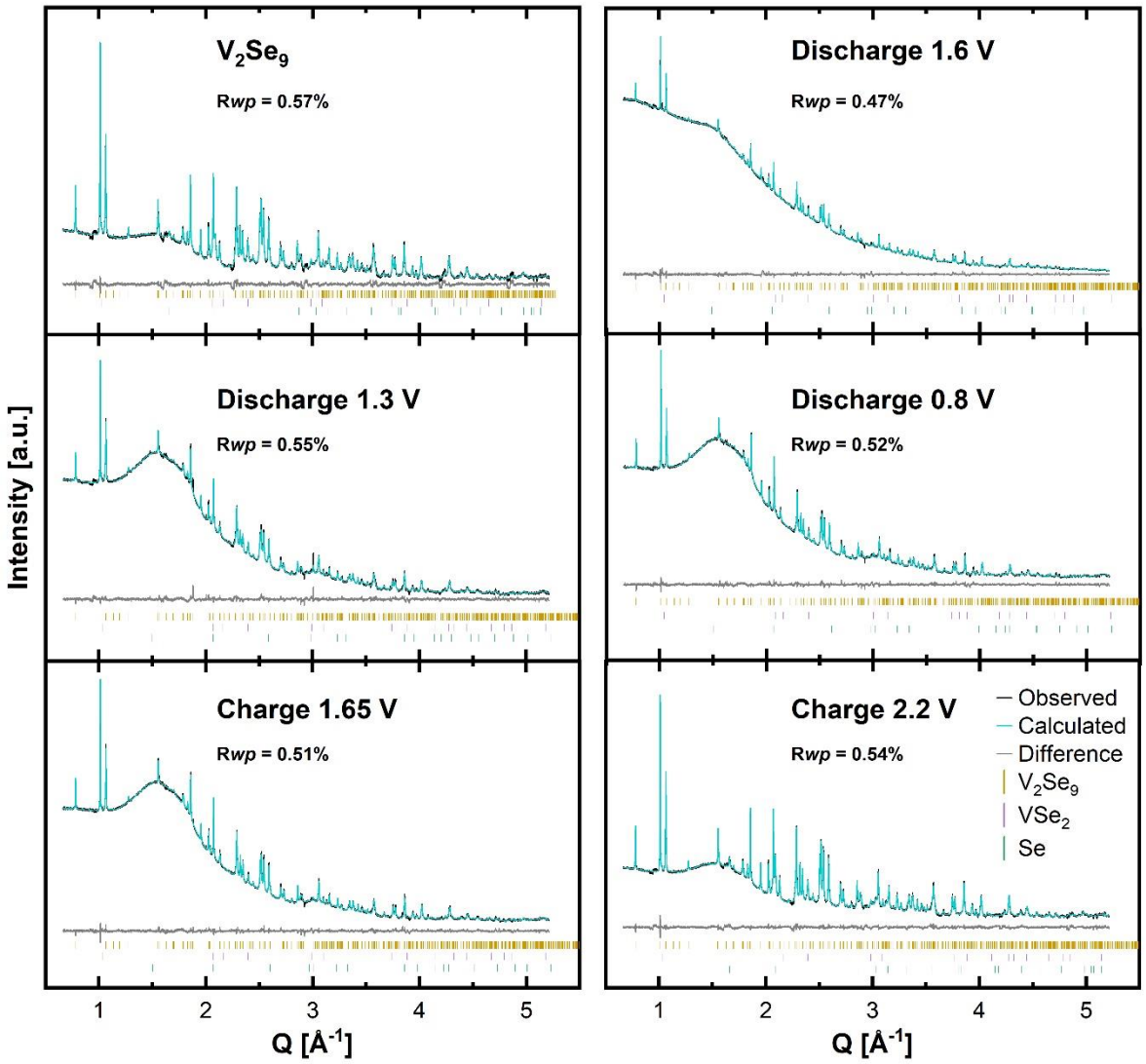

Figure S15 Rietveld refinement against SXRD data collected at the I11 beamline of $Mg_xV_2Se_9$ for samples taken at 1.6 V (x = 0.15); 1.3 V (x = 0.47); and 0.8 V (x = 1.35), 1.65 V (x = 0.97) and 2.2 V (x = 0.00). Observed data are shown by white circles. The calculated fit is shown by the cyan line. The difference between the calculated and observed data is shown by the grey line. The reflection positions of V_2Se_9, VSe_2 and Se are given by the gold, purple and green ticks, respectively. Refined parameters are summarized in Tables S2, S7, and S8-11.

Table S8 Rietveld parameters for $Mg_{0.10}V_2Se_9$ (discharged to 1.6 V) with refined lattice parameters, atomic coordinates, and isotropic displacement parameters against SXRD. The total refined Mg content is 0.28(3).

C 2/*c*		R_{wp} = 0.47%		R_p = 0.31%	G.O.F = 3.51		
Atom	Oxidation	Wykoff	x	y	z	Occ	B_{iso} (Å^2)
Mg1	Mg^{2+}	4a	0	0.5	0	0.22(3)	2.9(2)
Mg2	Mg^{2+}	4b	0.5	0.5	0	0.06(3)	2.9(2)
V1	V^{5+}	8f	0.1252(8)	0.2295(4)	0.4102(10)	1.00	1.34(19)
Se1	Se^{2-}	4e	0	0.0834(7)	0.25	1.00	0.8(2)
Se2	Se^{1-}	8f	0.4381(4)	0.3473(4)	0.0404(6)	1.00	0.95(16)
Se3	Se^{1-}	8f	0.1061(4)	0.3096(4)	0.1098(5)	1.00	1.53(18)
Se4	Se^{1-}	8f	0.2632(4)	0.0900(5)	0.5575(6)	1.00	0.90(17)
Se5	Se^{1-}	8f	0.3317(5)	0.1605(4)	0.3190(6)	1.00	1.28(16)

a = 10.57679(15) Å

b = 12.3961(2) Å

c = 8.11068(11) Å

β = 94.9127(11)°

Volume = 1059.49(3) Å^3

Table S9 Rietveld parameters for $Mg_{0.41}V_2Se_9$ (discharged to 1.3 V) with refined lattice parameters, atomic coordinates, and isotropic displacement parameters against SXRD. The total refined Mg content is 0.81(2).

C 2/*c*		R_{wp} = 0.55%		R_p = 0.38%		G.O.F = 5.56	
Atom	Oxidation	Wykoff	x	y	z	Occ	B_{iso} (Å^2)
Mg1	Mg^{2+}	4a	0	0.5	0	0.553(14)	3.0(2)
Mg2	Mg^{2+}	4b	0.5	0.5	0	0.263(14)	3.0(2)
V1	V^{5+}	8f	0.1252(8)	0.2295(4)	0.4102(9)	1.00	1.34(18)
Se1	Se^{2-}	4e	0	0.0834(7)	0.25	1.00	0.8(2)
Se2	Se^{1-}	8f	0.4381(4)	0.3473(3)	0.0404(6)	1.00	0.95(17)
Se3	Se^{1-}	8f	0.1061(4)	0.3096(3)	0.1098(5)	1.00	1.53(19)
Se4	Se^{1-}	8f	0.2632(3)	0.0900(4)	0.5575(6)	1.00	0.90(18)
Se5	Se^{1-}	8f	0.3317(5)	0.1605(3)	0.3190(7)	1.00	1.28(17)

a = 10.5772(2) Å

b = 12.3971(3) Å

c = 8.11105(16) Å

β = 94.9249(16)°

Volume = 1059.66(4) Å^3

Table S10 Rietveld parameters for $Mg_{0.97}V_2Se_9$ (charged to 1.65 V) with refined lattice parameters, atomic coordinates, and isotropic displacement parameters against SXRD. The total refined Mg content is 0.747(19).

C 2/*c*		R_{wp} = 0.51%		R_p = 0.36%		G.O.F = 3.77	
Atom	Oxidation	Wykoff	x	y	z	Occ	B_{iso} (Å^2)
Mg1	Mg^{2+}	4a	0	0.5	0	0.47(2)	2.5(3)
Mg2	Mg^{2+}	4b	0.5	0.5	0	0.27(2)	2.5(3)
V1	V^{5+}	8f	0.1252(6)	0.2295(3)	0.4102(7)	1.00	1.34(13)
Se1	Se^{2-}	4e	0	0.0834(5)	0.25	1.00	0.8(2)
Se2	Se^{1-}	8f	0.4381(3)	0.3473(2)	0.0404(4)	1.00	0.95(12)
Se3	Se^{1-}	8f	0.1061(3)	0.3096(2)	0.1098(3)	1.00	1.53(14)
Se4	Se^{1-}	8f	0.2632(2)	0.0900(3)	0.5575(4)	1.00	0.90(13)
Se5	Se^{1-}	8f	0.3317(4)	0.1605(3)	0.3190(4)	1.00	1.28(12)

a = 10.57699(12) Å

b = 12.3964(2) Å

c = 8.11045(10) Å

β = 94.9144(9)°

Volume = 1059.51(2) Å^3

Table S11 Rietveld parameters for $Mg_{0.0}V_2Se_9$ (charged to 2.2 V) with refined lattice parameters, atomic coordinates, and isotropic displacement parameters against SXRD. The occupancy of Mg1 & Mg2 are within error of zero, 0.03(2), and atomic displacement parameters could not be refined to sensible values for these positions; suggesting Mg is removed from these sites during charging to 2.2 V.

C 2/*c*		R_{wp} = 0.54%		R_p = 0.39%		G.O.F = 6.18	
Atom	Oxidation	Wykoff	x	y	z	Occ	B_{iso} (Å^2)
Mg1	Mg^{2+}	4a	0	0.5	0	0.031(17)	-
Mg2	Mg^{2+}	4b	0.5	0.5	0	0.000(11)	-
V1	V^{5+}	8f	0.1307(4)	0.2327(2)	0.4106(5)	1.00	0.30(9)
Se1	Se^{2-}	4e	0	0.0865(3)	0.25	1.00	1.19(14)
Se2	Se^{1-}	8f	0.4409(2)	0.3487(2)	0.0391(3)	1.00	1.28(8)
Se3	Se^{1-}	8f	0.1018(2)	0.3140(2)	0.1087(2)	1.00	0.96(9)
Se4	Se^{1-}	8f	0.2613(2)	0.0826(2)	0.5563(3)	1.00	1.04(9)
Se5	Se^{1-}	8f	0.3372(2)	0.1592(2)	0.3225(3)	1.00	0.78(9)

a = 10.58856(6) Å

b = 12.40910(7) Å

c = 8.11997(6) Å

β = 94.9208(7)°

Volume = 1062.988(13) Å^3

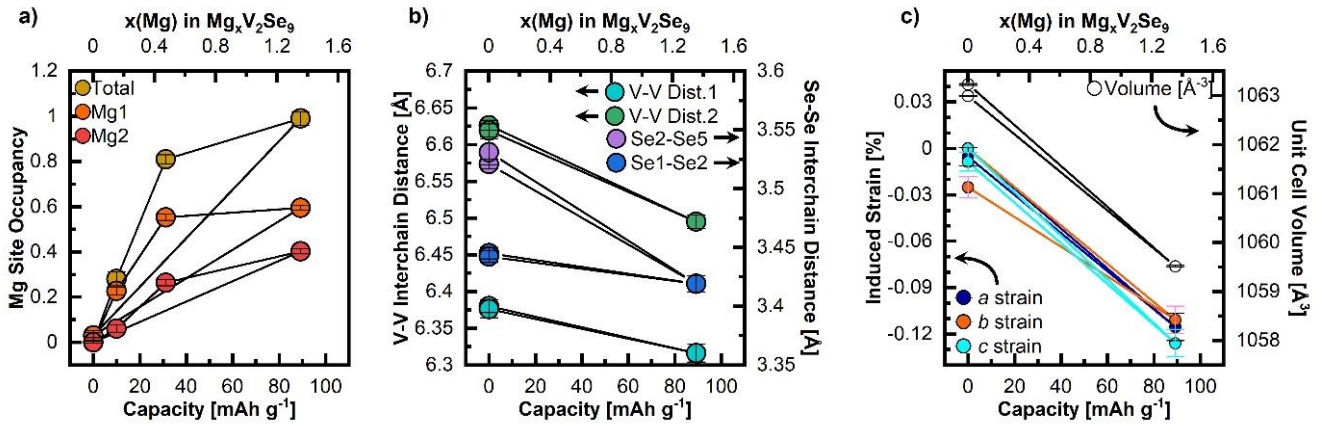

Figure S16 (a) Refined Mg(1), Mg(2) and total Mg occupancies within $Mg_xV_2Se_9$ (per formula unit, considering Wyckoff position and site multiplicity within the unit cell, as a function of discharge capacity. (b) Inter-chain distances, in Å, for V–V centres along [001] (light blue) and [011] (green) and Se–Se centres (see figure S1). (c) Induced %strain for lattice parameters *a* (dark blue), *b* (orange) and *c* (cyan) as a function of capacity for V_2Se_9, $Mg_{1.35}V_2Se_9$ (discharged to 0.8 V) and $Mg_{0.0}V_2Se_9$ (charged to 2.2 V). Unit cell volume change is shown in black.

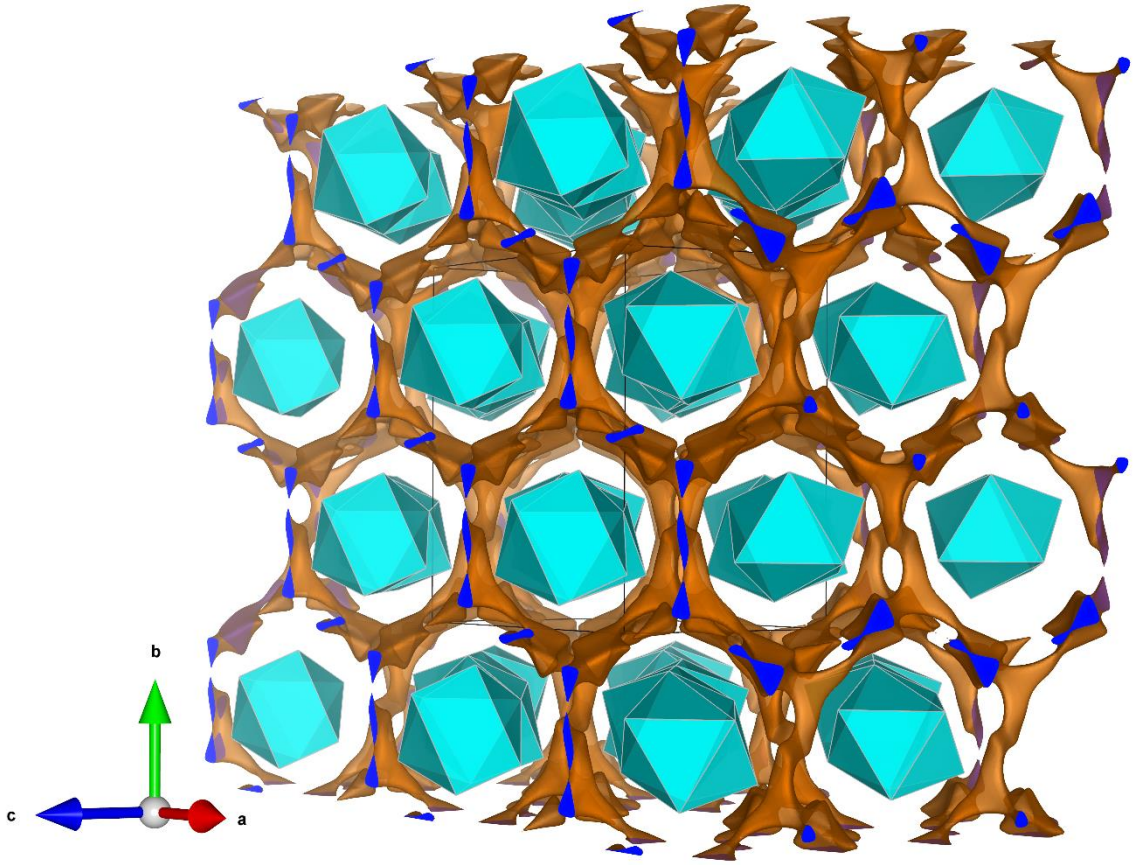

Figure S17 Migration pathways (orange isosurface - shown at 5 $bohr^{-3}$) calculated for Mg^{2+} through bulk V_2Se_9 (blue polyhedra) as calculated by BVPA.

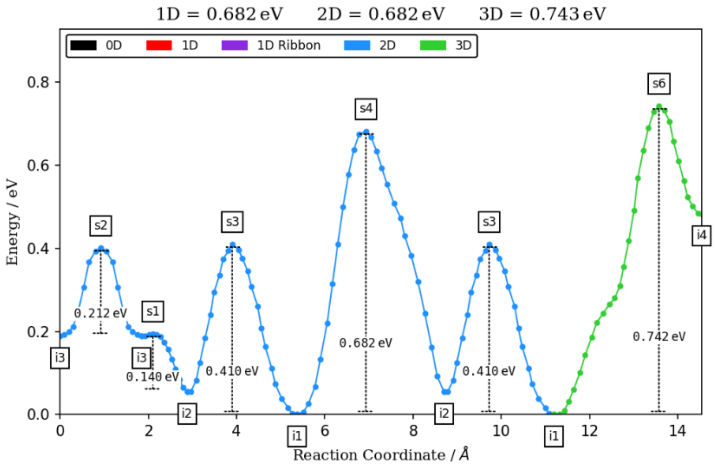

Figure S18 Migration barriers for Mg^{2+} ion conduction in V_2Se_9 as calculated by BVPA.

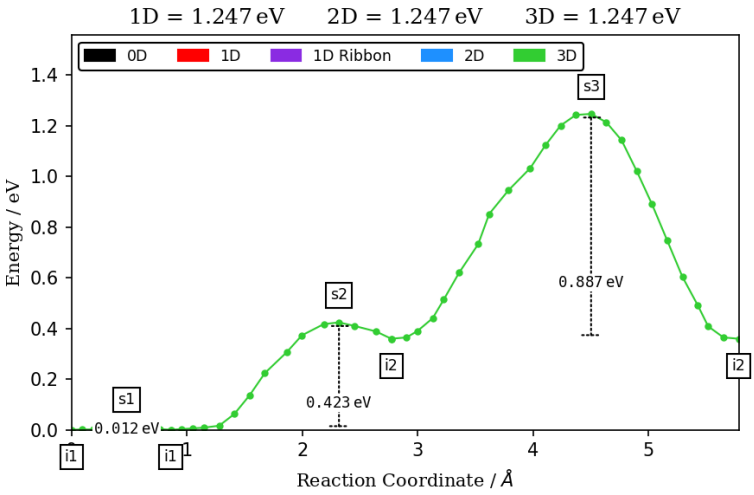

Figure S19 Migration barriers for Mg^{2+} ion conduction in Mo_6S_8 as calculated by BVPA.

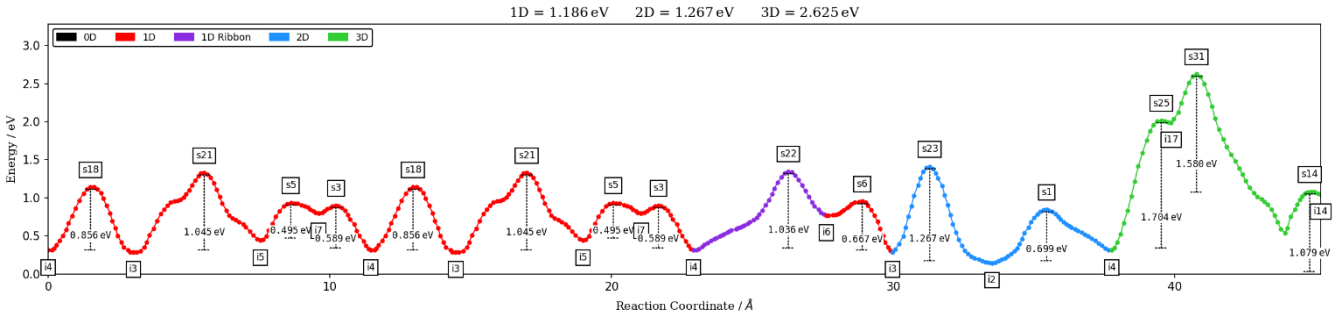

Figure S20 Migration barriers for Mg^{2+} ion conduction in V_2PS_{10} calculated by BVPA.

Table S12 Interatomic distances in $Mg_xV_2Se_9$ for $0 \leq x \leq 1.35$. Period refers to the distance (Å) of one translation period along the V_2Se_9 chains between crystallographically identical V sites.

BOND	OCV (1.9 V) V2Se9	1.6 V (Dis) $Mg_{0.15}V_2Se_9$	1.3 V (Dis) $Mg_{0.47}V_2Se_9$	0.8 V (Dis) $Mg_{1.35}V_2Se_9$	1.65 V (Ch) $Mg_{0.97}V_2Se_9$	2.2 V (Ch) $Me_{0.0}V_2Se_9$
PERIOD	12.77923(16)	12.7655(2)	12.7647(3)	12.76535(15)	12.76535(17)	12.77893(10)
V-V'	2.802(9)	2.946(18)	2.945(17)	2.946(11)	2.946(12)	2.837(10)
V-V"	3.671(8)	3.551(17)	3.550(16)	3.550(11)	3.550(12)	3.637(10)
Se2-Se3	2.375(4)	2.322(7)	2.322(7)	2.322(5)	2.322(6)	2.374(4)
Se4-Se5	2.329(5)	2.296(8)	2.296(6)	2.296(6)	2.296(6)	2.328(4)
Se4-Se5'	3.543(4)	3.425(8)	3.426(8)	3.426(6)	3.426(7)	3.534(4)
Se1-Se2	2.618(4)	2.642(6)	2.643(7)	2.642(4)	2.642(5)	2.607(3)
Se1-V	2.583(5)	2.536(10)	2.536(10)	2.536(7)	2.536(7)	2.568(5)
Se2-V	3.814(6)	3.782(10)	3.782(10)	3.782(7)	3.782(7)	3.802(5)
Se2-V'	2.560(6)	2.510(11)	2.510(10)	2.510(7)	2.510(8)	2.552(6)
Se3-V	2.645(5)	2.623(10)	2.624(9)	2.623(7)	2.623(7)	2.644(5)
Se3-V'	2.675(5)	2.634(11)	2.634(10)	2.634(7)	2.634(7)	2.654(6)
Se4-V	2.561(4)	2.531(10)	2.531(9)	2.531(6)	2.531(7)	2.565(5)
Se4-V'	2.534(5)	2.499(10)	2.499(9)	2.499(6)	2.499(7)	2.550(5)
Se5-V	2.545(5)	2.591(10)	2.591(10)	2.591(7)	2.591(7)	2.545(5)
Se5-V'	2.523(6)	2.514(12)	2.514(10)	2.514(7)	2.514(8)	2.529(6)

Table S13 Character Table for C_{2h} (2/*m*)

C_2h (2/*m*)		1	2	–1	m	Functions
A_g	Γ_1^+	1	1	1	1	x^2, y^2, z^2, xz, J_y
B_g	Γ_2^+	1	–1	1	–1	xy, yz, J_x, J_z
A_u	Γ_1^-	1	1	–1	–1	y
B_u	Γ_2^-	1	–1	–1	1	x, z

Table S14 Raman Tensors in C_{2h} (2/*m*)

A_g			B_g		
b	▪	d	▪	f	▪
▪	c	▪	f	▪	e
d	▪	a	▪	e	▪

Table S15 Raman active modes in C_{2h} (2/*m*)

Wyckoff	A_g	A_u	B_g	B_u
4a	▪	▪	▪	▪
4b	▪	▪	▪	▪
4e	1	▪	2	▪
8f	3	▪	3	▪

Table S16 Raman modes observed in V_2Se_9, $Mg_{1.35}V_2Se_9$ (0.8 V) and V_2Se_9 (Ch 2.2 V)

V_2Se_9			$Mg_{1.35}V_2Se_9$ (0.8 V)		V_2Se_9 (Ch 2.2 V)	
[cm^{-1}]	Norm. Int.	FWHM [cm^{-1}]	cm^{-1}	Norm. Int.	cm^{-1}	Norm. Int.
108	0.79	6.7	106	1.00	107	0.76
120	0.64	10.1	116	0.48	116	0.33
			122	0.44	122	0.31
			129	0.42	131	0.19
136	0.39	6.3	139	0.62	139	0.44
150	0.52	10.1	146	0.26	146	0.10
175	0.42	9.2	155	0.33	153	0.17
197	0.10	9.5			193	0.38
269	0.36	11.1	267	0.31	269	0.32
295	0.83	15.6			297	0.15
315	0.73	12.3	311	0.24	315	0.52
330	0.47	12.9			330	0.70
346	1.00	9.2	339	0.41	340	1.00

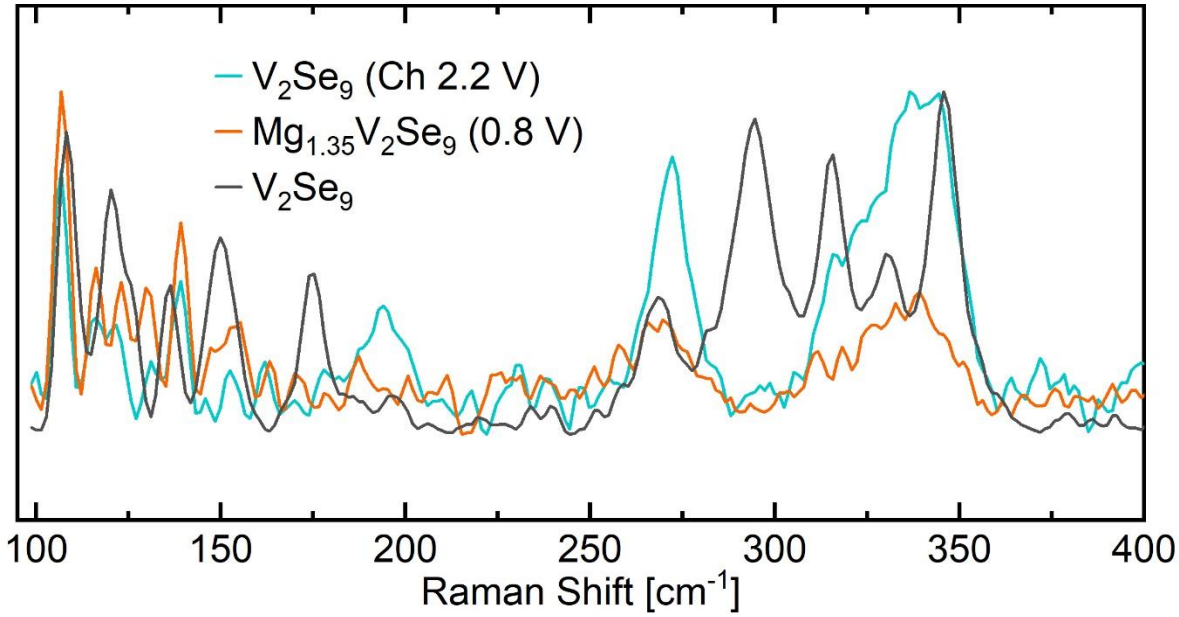

Figure S21 Overlaid Raman noramalized spectra for V_2Se_9 (grey), $Mg_{1.35}V_2Se_9$ (discharged 0.8 V, orange), and V_2Se_9 (charged 2.2 V, cyan). Spectra have been normalized to their most intense peak and backgrounds removed.

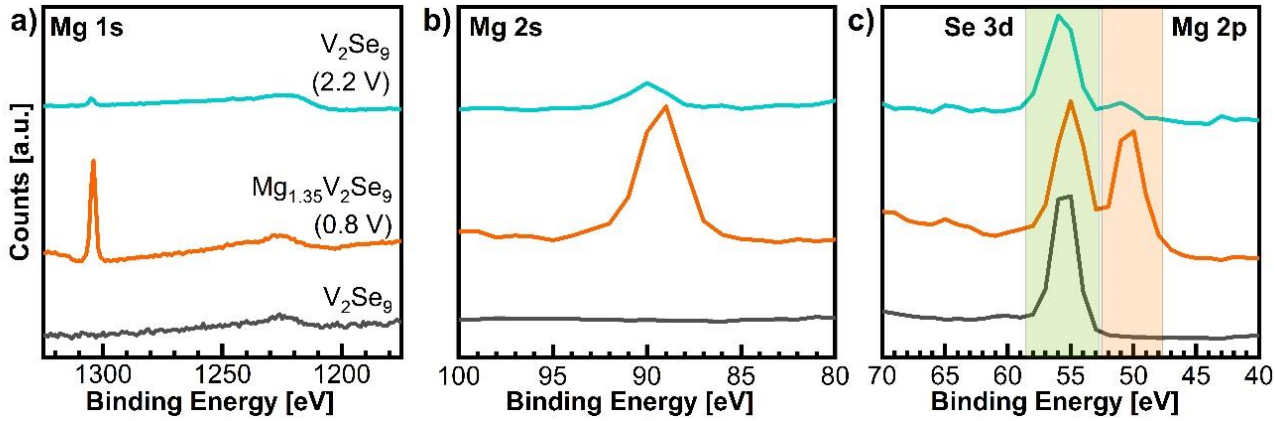

Figure S22 Mg XPS survey spectra collected at a pass energy of 200 eV for V_2Se_9 (dark grey), $Mg_{1.35}V_2Se_9$ (discharged to 0.8 V, orange curve), and V_2Se_9 (charged to 2.2 V, blue curve) for a) the Mg 1s region (1303.2 eV), b) Mg 2s region (89.0 eV), and c) the Mg 2p region (49.8 eV). The spectra have been scaled to the Se 3d signal (55.4 eV).

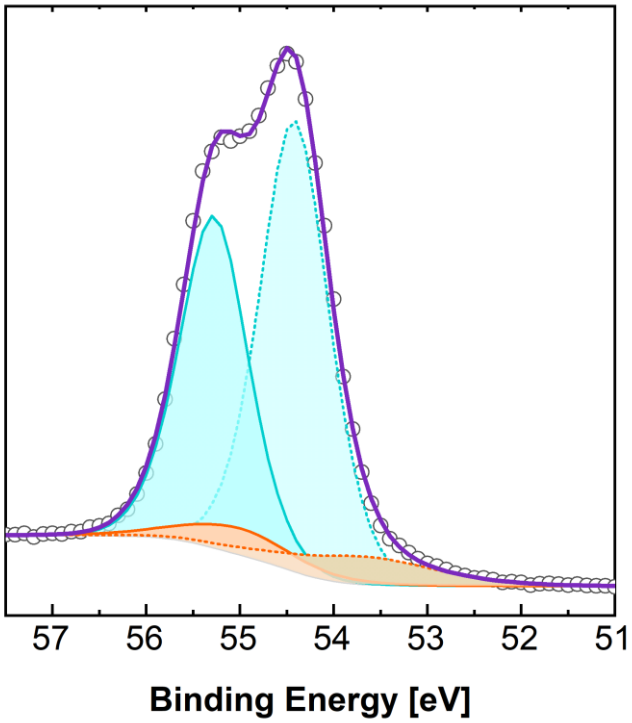

Figure S23 Se 3d XPS collected at a pass energy of 40 eV. Both Se 3d5/2 and Se 3d3/2 contributions are shown for each Se species: $(Se_2)^{2-}$ and Se^{2-}. The sum of orbital contributions is shown as the gold envelope relative to the observed data (black line). The Se 3d5/2 and 3d3/2 spin-orbit components of each oxidation state were constrained based on relative position, $\Delta = 0.86$ eV, and intensity ratio = 0.735. The relative areas of $Se^{2-}/(Se_2)^{2-}$ for V_2Se_9 were constrained to reflect the nominal formula $V_2^{5+}(Se_2)^{2-}{}_4Se^{2-}$.

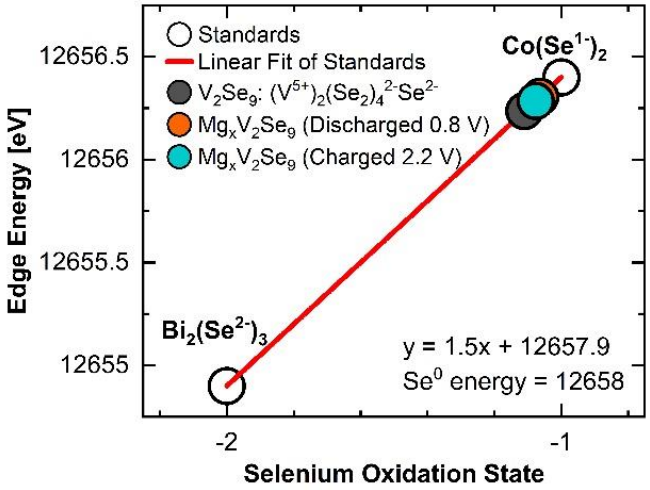

Figure S24 Se K-edge positions of V_2Se_9, $Mg_{1.35}V_2Se_9$ (discharged to 0.8 V) and V_2Se_9 (charged to 2.2 V) plotted along a calibration curve formed the edge positions of standards $Co(Se^{1-})_2$ and $Bi_2(Se^{2-})_3$ calibrated with an internal Se^0 reference foil.

References

(1) Meerschaut, A.; Guemas, L.; Berger, R.; J, R. The Crystal Structure of Niobium Selenide Nb2Se9 from Twin-Crystal Data. *Acta Crystallogr. Sect. B* **1979**, *35* (8), 1747–1750. https://doi.org/10.1107/S0567740879007688.

(2) Brown, D. I. The Chemical Bond in Inorganic Chemistry: The Bond Valence Model, 2nd Ed. *J. Mater. Sci.* **2017**, *52* (17), 9959–9962. https://doi.org/10.1007/s10853-017-1215-2.

(3) Brese, N. E.; O'Keeffe, M. Bond-Valence Parameters for Solids. *Acta Crystallogr. Sect. B* **1991**, *47* (2), 192–197. https://doi.org/10.1107/S0108768190011041.

(4) J L Hodeau; M Marezio; C Roucau; R Ayroles; A Meerschaut; J Rouxel; P Monceau. Charge-Density Waves in NbSe3 at 145K: Crystal Structures, X-Ray and Electron Diffraction Studies. *J. Phys. C Solid State Phys.* **1978**, *11* (20), 4117. https://doi.org/10.1088/0022-3719/11/20/009.

(5) Meerschaut, A.; Guemas, L.; Berger, R.; Rouxel, J. The Crystal Structure of Niobium Selenide Nb2Se9 from Twin-Crystal Data. *Acta Crystallogr. Sect. B* **1979**, *35* (8), 1747–1750. https://doi.org/10.1107/S0567740879007688.

(6) Wright, M. A.; Surta, T. W.; Evans, J. A.; Lim, J.; Jo, H.; Hawkins, C. J.; Bahri, M.; Daniels, L. M.; Chen, R.; Zanella, M.; Chagas, L. G.; Cookson, J.; Collier, P.; Cibin, G.; Chadwick, A. V.; Dyer, M. S.; Browning, N. D.; Claridge, J. B.; Hardwick, L. J.; Rosseinsky, M. J. Accessing Mg-Ion Storage in V2PS10 via Combined Cationic-Anionic Redox with Selective Bond Cleavage. *Angew. Chemie Int. Ed.* **2024**, e202400837. https://doi.org/10.1002/ANIE.202400837.

(7) Pise, M. T.; Srinivas, S.; Chatterjee, A.; Kashyap, B. P.; Singh, R. N.; Tatiparti, S. S. V. Influence of Surface Condition on the Current Densities Rendering Nucleation Loop during Cyclic Voltammetry for Electrodeposition of Pd Thin Films. *Surf. Interfaces* **2020**, *20*, 100525. https://doi.org/https://doi.org/10.1016/j.surfin.2020.100525.

(8) Hou, S.; Ji, X.; Gaskell, K.; Wang, P.-F.; Wang, L.; Xu, J.; Sun, R.; Borodin, O.; Wang, C. Solvation Sheath Reorganization Enables Divalent Metal Batteries with Fast Interfacial Charge Transfer Kinetics. *Science* **2021**, *374* (6564), 172–178. https://doi.org/10.1126/science.abg3954.